Analysis of Vectorial Mode Fields in Optical Waveguides by a New Finite Difference Method

P. Lüsse, *Student Member, IEEE,* P. Stuwe, *Member, IEEE,* J. Schüle, and H.-G. Unger, *Life Fellow, IEEE*

***Abstract*—An important class of dielectric optical waveguides has stepped refractive index profiles. For these waveguides we present a new finite-difference approach free of spurious modes. The coupled difference equations are formulated in terms of the transverse magnetic field components H_x and H_y. We show how the boundary conditions can be formulated and included in the finite difference scheme to obtain a unique set of equations. For a step-index fiber a comparison of the numerical results with the analytical solution shows that the relative error in the propagation constant is as low as 4.4×10^{-7} for an index difference of 7.3%. For a rib waveguide, we compare our results with previously published data based on other methods. Field plots of the dominant *and* the weak transverse field components of the magnetic field for the fundamental mode of a buried rib waveguide are also given.**

I. Introduction

RECENT advances in semiconductor technology allow the integration of many optical and electronic components on a single substrate [1], [2]. These optoelectronic integrated circuits are key elements for applications ranging from communications to optical sensing. The design of waveguide components such as directional couplers, wavelength selective couplers or 3-dB couplers demands reliable numerical methods. The accuracy required in the calculation of the propagation constant of a mode for the design of such components can be estimated by the following consideration: Complex longitudinal homogeneous waveguide devices owe their function to the interference of several modes excited at the input port. The phase of each of these modes changes during propagation in z direction according to the propagation term $\exp(-j\beta_i z)$. For proper function of the device, the phase difference $\Delta\beta_{i,j}L = (\beta_i - \beta_j)L$ of all pairs of modes i, j has to be small compared to $\pi/2$. For a typical geometric length of 1 mm at a wavelength of 1.5 μm this leads to

$$\Delta n_{\text{eff}} = \Delta\beta/k \ll \pi/(2kz) = 3.75 \cdot 10^{-4}. \qquad (1)$$

In this example the error in the computation of the effective refractive index must be kept below 10^{-5}.

Theoretical research in the field of dielectric waveguides for applications in integrated optics dates back to Schlosser [3] and Goell [4]. Today, the effective-index method and its variations are good tools to estimate the general properties of a wide class of dielectric waveguides. However, often the solutions are not accurate enough. Extensive research work has been carried out on finite-difference methods (e.g. [5], [6]) and it has been found that in the H_x,H_y-approach, spurious modes do not occur [7]. Scalar, semivectorial, and also vectorial methods have been developed. But to our knowledge, the numerical results have not yet been compared with an analytical solution, as is possible for a step-index fiber. In Section III.1 we show that for this case a relative error of approximately 4.4×10^{-7} can be achieved for an index difference of 7.3%, which satisfies the requirements outlined in the last paragraph. Another extension to existing finite-difference schemes is the high numerical stability and dynamic range of our method, which allows the weak transverse component of the vector field of dielectric waveguides to be calculated with high accuracy. Preliminary results of our method have been published in [8].

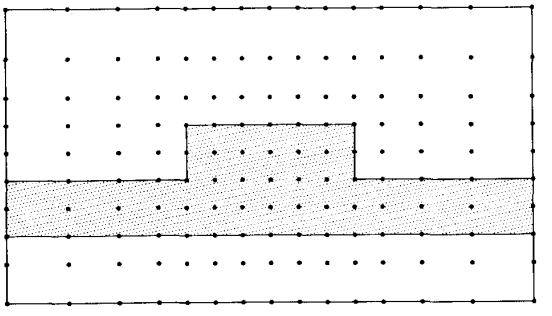

Fig. 1. Sketch of the discretization points of a ridge waveguide. The computational area may be limited by a Dirichlet or Neumann condition, an electric or a magnetic wall or a zero-condition.

II. Theory

A simple example of a dielectric waveguide is shown in Fig. 1. The structure is first scanned with points of a rectangular grid. In our finite-difference approach, it is essential that all dielectric boundaries are scanned by points of the grid that must lie exactly on the respective boundary. The general situation for an arbitrary point P inside the mesh with neighboring points N, W, S, E is shown in Fig. 2.

Since the four subregions (ν = 1, 2, 3, 4) in Fig. 2 are homogeneous, the Helmholtz equations

$$\frac{\partial^2 H_x}{\partial x^2} + \frac{\partial^2 H_x}{\partial y^2} + (\epsilon_\nu k^2 - \beta^2)H_x = 0 \qquad (2)$$

$$\frac{\partial^2 H_y}{\partial x^2} + \frac{\partial^2 H_y}{\partial y^2} + (\epsilon_\nu k^2 - \beta^2)H_y = 0 \qquad (3)$$

Manuscript received June 6, 1993; revised November 8, 1993.

P. Lüsse, P. Stuwe, and H.-G. Unger are with the Institut für Hochfrequenztechnik, Technische Universität Braunschweig, 38023 Braunschweig, Germany.

J. Schüle is with the Rechenzentrum, Technische Universität Braunschweig, 38023 Braunschweig, Germany.

IEEE Log Number 9215936D.

0733–8724/94$04.00 © 1994 IEEE

Authorized licensed use limited to: CAMBRIDGE UNIV. Downloaded on May 25,2020 at 12:09:14 UTC from IEEE Xplore. Restrictions apply.

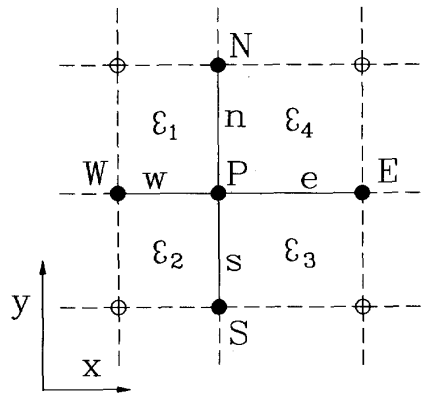

Fig. 2. Point P and neighboring points in a cartesian mesh with uniform dielectric constants ϵ_1,ϵ_2, ϵ_3 and ϵ_4 of the subregions 1–4.

are valid *inside* each of these regions. To derive two coupled difference equations for H_x and H_y, we first substitute the second derivatives $\partial^2 H_x/\partial x^2$ and $\partial^2 H_y/\partial y^2$ by a second order expansion at the point P. Two sets of four equations are obtained

$$\frac{2H_W}{w^2} - \frac{2H_P}{w^2} + \frac{2}{w}\frac{\partial H}{\partial x}\Big|_w + \frac{2H_N}{n^2} - \frac{2H_P}{n^2} - \frac{2}{n}\frac{\partial H}{\partial y}\Big|_n + \varepsilon_1 k^2 H_P = \beta^2 H_P, \tag{4}$$

$$\frac{2H_W}{w^2} - \frac{2H_P}{w^2} + \frac{2}{w}\frac{\partial H}{\partial x}\Big|_w + \frac{2H_S}{s^2} - \frac{2H_P}{s^2} + \frac{2}{s}\frac{\partial H}{\partial y}\Big|_s + \varepsilon_2 k^2 H_P = \beta^2 H_P, \tag{5}$$

$$\frac{2H_E}{e^2} - \frac{2H_P}{e^2} - \frac{2}{e}\frac{\partial H}{\partial x}\Big|_e + \frac{2H_S}{s^2} - \frac{2H_P}{s^2} + \frac{2}{s}\frac{\partial H}{\partial y}\Big|_s + \varepsilon_3 k^2 H_P = \beta^2 H_P, \tag{6}$$

$$\frac{2H_E}{e^2} - \frac{2H_P}{e^2} - \frac{2}{e}\frac{\partial H}{\partial x}\Big|_e + \frac{2H_N}{n^2} - \frac{2H_P}{n^2} - \frac{2}{n}\frac{\partial H}{\partial y}\Big|_n + \varepsilon_4 k^2 H_P = \beta^2 H_P, \tag{7}$$

where H denotes H_x for (2) or H_y for (3). In the next sections we show how these eight equations are combined and reduced to a set of two coupled equations by properly formulated boundary conditions.

A. Boundary Conditions

The two longitudinal components H_z and E_z are continuous at the horizontal and vertical interfaces of Fig. 3. H_z can be calculated from the transverse magnetic field components by

$$H_z = \frac{1}{j\beta}\left\{\frac{\partial H_x}{\partial x} + \frac{\partial H_y}{\partial y}\right\}, \tag{8}$$

which follows directly from

$$\mathrm{div}\vec{H} = 0. \tag{9}$$

It is necessary to consider the last equation to overcome the problems of spurious modes [9], [10]. With (8) this can be done in form of a boundary condition. With Maxwell's equation

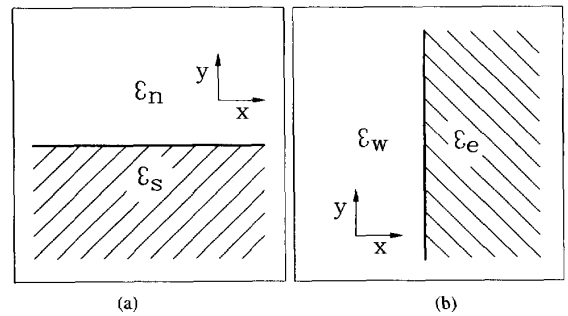

Fig. 3. (a) horizontal and (b) vertical dielectric boundary in cartesian coordinates.

$\mathrm{curl}\vec{H} = j\omega\varepsilon_0\varepsilon\ \vec{E}$ the component E_z can be expressed in terms of the transverse magnetic field:

$$E_z = \frac{1}{j\varepsilon k}\sqrt{\frac{\mu_0}{\varepsilon_0}}\left\{\frac{\partial H_y}{\partial x} - \frac{\partial H_x}{\partial y}\right\}. \tag{10}$$

We will first consider a horizontal boundary as shown in Fig. 3(a). Continuity of H_z from (8) at a horizontal boundary yields

$$\frac{\partial H_x}{\partial x}\Big|_n + \frac{\partial H_y}{\partial y}\Big|_n = \frac{\partial H_x}{\partial x}\Big|_s + \frac{\partial H_y}{\partial y}\Big|_s. \tag{11}$$

The indices n and s indicate that the the derivatives have to be taken in the respective half planes at an infinitesimal distance from the interface. Because of the uniqueness of the field along the boundary, the derivative with respect to x is equal in both half planfes. Therefore, (11) simplifies to

$$\frac{\partial H_y}{\partial y}\Big|_n = \frac{\partial H_y}{\partial y}\Big|_s. \tag{12}$$

The continuity of E_z at a horizontal boundary yields with (10)

$$\frac{1}{\varepsilon_n}\frac{\partial H_y}{\partial x}\Big|_n - \frac{1}{\varepsilon_n}\frac{\partial H_x}{\partial y}\Big|_n = \frac{1}{\varepsilon_s}\frac{\partial H_y}{\partial x}\Big|_s - \frac{1}{\varepsilon_s}\frac{\partial H_x}{\partial y}\Big|_s. \tag{13}$$

Again derivatives with respect to x are equal in both half planes and hence we can drop the indices s and n for them. By rearranging (13) we obtain

$$\varepsilon_n\frac{\partial H_x}{\partial y}\Big|_s - \varepsilon_s\frac{\partial H_x}{\partial y}\Big|_n = (\varepsilon_n - \varepsilon_s)\frac{\partial H_y}{\partial x}. \tag{14}$$

At a vertical boundary we can derive equations in a similar way. Here, continuity of H_z yields

$$\frac{\partial H_x}{\partial x}\Big|_w = \frac{\partial H_x}{\partial x}\Big|_e \tag{15}$$

and continuity of E_z:

$$\varepsilon_e\frac{\partial H_y}{\partial x}\Big|_w - \varepsilon_w\frac{\partial H_y}{\partial x}\Big|_e = (\varepsilon_e - \varepsilon_w)\frac{\partial H_x}{\partial y}. \tag{16}$$

Authorized licensed use limited to: CAMBRIDGE UNIV. Downloaded on May 25,2020 at 12:09:14 UTC from IEEE Xplore. Restrictions apply.

B. Formulation of the Difference Equations

With the four boundary conditions (12), (14), (15), and (16), equations (4)–(7) can be combined to obtain the desired coupled difference equations for H_x and H_y.

First we consider (4)–(7) with $H = H_x$. The subregions 1 and 2 in Fig. 2 are separated by a horizontal boundary. Adding (4) multiplied by $\varepsilon_2 n/2$, and (5) multiplied by $\varepsilon_1 s/2$, gives an equation containing the left hand side of (14). Substituting this term by the right hand side of (14) yields

$$\begin{aligned}&\frac{s\varepsilon_1+n\varepsilon_2}{w^2}H_{xw}-\frac{s\varepsilon_1+n\varepsilon_2}{w^2}H_xP+\frac{s\varepsilon_1+n\varepsilon_2}{w}\frac{\partial H_x}{\partial x}\Big|_w\\&+\frac{\varepsilon_2}{n}H_{xN}+\frac{\varepsilon_1}{s}H_{xS}-\frac{n\varepsilon_1+s\varepsilon_2}{ns}H_{xP}\\&+(\varepsilon_1-\varepsilon_2)\frac{\partial H_y}{\partial x}+\frac{\varepsilon_1\varepsilon_2(n+s)}{2}k^2H_{xP}\\&=\frac{s\varepsilon_1+n\varepsilon_2}{2}\beta^2H_{xP}.\end{aligned}\tag{17}$$

The equations (6) and (7) for the subregions 3 and 4 in Fig. 2 can be combined in a similar way: After multiplying (6) by $\varepsilon_4 s/2$ and (7) by $\varepsilon_3 n/2$ and adding these two equations, we obtain

$$\begin{aligned}&\frac{n\varepsilon_3+s\varepsilon_4}{e^2}H_{xE}-\frac{n\varepsilon_3+s\varepsilon_4}{e^2}H_{xP}-\frac{n\varepsilon_3+s\varepsilon_4}{e}\frac{\partial H_x}{\partial x}\Big|_e\\&+\frac{\varepsilon_3}{n}H_{xN}+\frac{\varepsilon_4}{s}H_{xS}-\frac{s\varepsilon_3+n\varepsilon_4}{ns}H_{xP}\\&+(\varepsilon_4-\varepsilon_3)\frac{\partial H_y}{\partial x}+\frac{\varepsilon_3\varepsilon_4(n+s)}{2}k^2H_{xP}\\&=\frac{n\varepsilon_3+s\varepsilon_4}{2}\beta^2H_{xP},\end{aligned}\tag{18}$$

where the boundary condition (14) has also been considered.

Next we multiply (17) by $w/(s\varepsilon_1+n\varepsilon_2)$ and (18) by $e/(n\varepsilon_3+s\varepsilon_4)$ and add them. This procedure results in the desired difference equation for H_x:

$$\begin{aligned}&\frac{2H_{xE}}{e(e+w)}+\frac{2H_{xS}(e\varepsilon_4(s\varepsilon_1+n\varepsilon_2)+w\varepsilon_1(n\varepsilon_3+s\varepsilon_4))}{s(s\varepsilon_1+n\varepsilon_2)(n\varepsilon_3+s\varepsilon_4)(e+w)}\\&+\frac{2H_{xW}}{e(e+w)}+\frac{2H_{xN}(e\varepsilon_3(s\varepsilon_1+n\varepsilon_2)+w\varepsilon_2(n\varepsilon_3+s\varepsilon_4))}{n(s\varepsilon_1+n\varepsilon_2)(n\varepsilon_3+s\varepsilon_4)(e+w)}\\&+2\left(\frac{e(\varepsilon_4-\varepsilon_3)}{(n\varepsilon_3+s\varepsilon_4)(e+w)}+\frac{w(\varepsilon_1-\varepsilon_2)}{(s\varepsilon_1+n\varepsilon_2)(e+w)}\right)\\&\cdot\left(\frac{wH_{yE}}{e(e+w)}+\frac{(e-w)H_yP}{ew}-\frac{eH_{yW}}{w(e+w)}\right)-H_xP\left(\frac{2}{ew}+\right.\\&2\frac{e(s\varepsilon_1+n\varepsilon_2)(\varepsilon_3/x+\varepsilon_4/s)+w(n\varepsilon_3+s\varepsilon_4)(\varepsilon_1/s+\varepsilon_2/n)}{(s\varepsilon_1+n\varepsilon_2)(n\varepsilon_3+s\varepsilon_4)(e+w)}\\&\left.-\frac{k^2(n+s)(e\varepsilon_3\varepsilon_4(s\varepsilon_1+n\varepsilon_2)+w\varepsilon_1\varepsilon_2(n\varepsilon_3+s\varepsilon_4))}{(s\varepsilon_1+n\varepsilon_2)(n\varepsilon_3+s\varepsilon_4)(e+w)}\right)\\&=\beta^2H_{yP}.\end{aligned}\tag{19}$$

In the last step the boundary condition (12) and the central difference quotient [11]

$$\frac{\partial H_y}{\partial x}=\frac{wH_{yE}}{e(e+w)}+\frac{(e-w)H_yP}{ew}-\frac{eH_{yW}}{w(e+w)}\tag{20}$$

were used.

To derive the difference equation for H_y, we again start with (4)–(7), where now $H = H_y$. Equations (4) and (7), representing the regions 1 and 4 in Fig. 2, are combined by multiplying (4) with $w\varepsilon_4/2$ and adding the result to (7) multiplied by $e\varepsilon_1/2$. The derivatives of H_y with respect to x are then replaced by the righthand side of the boundary condition (16). In a similar way we derive an equation for the lower half plane of the Fig. 2. Here (5) has to be multiplied by $w\varepsilon_3/2$ and (6) by $e\varepsilon_2/2$. Adding the two equations and substituting the boundary condition (16) yields an equation for the upper half plane. The equations for the lower and lower half planes are then combined by multiplying the last by $n/(e\varepsilon_1+w\varepsilon_4)$ and the latter by $s/(e\varepsilon_3+w\varepsilon_3)$. Adding the results yields the difference equation for H_y:

$$\begin{aligned}&\frac{2H_{yS}}{s(n+s)}+\frac{2H_{yE}(n\varepsilon_1(e\varepsilon_2+w\varepsilon_3)+s\varepsilon_2(e\varepsilon_1+w\varepsilon_4))}{e(e\varepsilon_2+w\varepsilon_3)(e\varepsilon_1+w\varepsilon_4)(n+s)}\\&+\frac{2H_{yN}}{n(n+s)}+\frac{2H_{yW}(n\varepsilon_4(e\varepsilon_2+w\varepsilon_3)+s\varepsilon_3(e\varepsilon_1+w\varepsilon_4))}{w(e\varepsilon_2+w\varepsilon_3)(e\varepsilon_1+w\varepsilon_4)(n+s)}\\&+2\left(\frac{n(\varepsilon_4-\varepsilon_1)}{(e\varepsilon_1+w\varepsilon_4)(n+s)}+\frac{s(\varepsilon_3-\varepsilon_2)}{(e\varepsilon_2+w\varepsilon_3)(n+s)}\right)\\&\cdot\left(\frac{sH_{xN}}{n(n+s)}+\frac{(n-s)H_{xP}}{ns}-\frac{nH_{xS}}{s(n+s)}\right)-H_{yP}\left(\frac{2}{ns}+\right.\\&2\frac{n(e\varepsilon_2+w\varepsilon_3)(\varepsilon_1/e+\varepsilon_4/w)+s(e\varepsilon_1+w\varepsilon_4)(\varepsilon_2/e+\varepsilon_3/w)}{(e\varepsilon_2+w\varepsilon_3)(e\varepsilon_1+w\varepsilon_4)(n+s)}\\&\left.-\frac{k^2(e+w)(n\varepsilon_1\varepsilon_4(e\varepsilon_2+w\varepsilon_3)+s\varepsilon_2\varepsilon_3(e\varepsilon_1+w\varepsilon_4))}{(e\varepsilon_2+w\varepsilon_3)(e\varepsilon_1+w\varepsilon_4)(n+s)}\right)\\&=\beta^2H_{yP}.\end{aligned}\tag{21}$$

In the last step we have made use of the boundary condition (15) and the central difference quotient

$$\frac{\partial H_x}{\partial y}=\frac{sH_{xN}}{n(n+s)}+\frac{(n-s)H_{xP}}{ns}-\frac{nH_{xS}}{s(n+s)}.\tag{22}$$

It is convenient to use some abbreviations in the coupled difference equations (19) and (21), resulting in

$$\begin{aligned}&a_{xxW}\,H_{xW}+a_{xxE}H_{xE}+a_{xxN}H_{xN}+a_{xxS}H_{xS}\\&+a_{xxP}H_{xP}+a_{xyW}H_{yW}+a_{xyP}H_{yP}+a_{xyE}H_{yE}=\beta^2H_{xP}\end{aligned}\tag{23}$$

and

$$\begin{aligned}&a_{yyW}H_{yW}+a_{yyE}H_{yE}+a_{yyN}H_{yN}+a_{yyS}H_{yS}\\&+a_{yyP}H_{yP}+a_{yxN}H_{xN}+a_{yxP}H_{xP}+a_{yxS}H_{xS}=\beta^2H_{yP}.\end{aligned}\tag{24}$$

Points P lying on the boundary of the computational window must be considered separately. Depending on the boundary condition used, Dirichlet, Neumann, electric or magnetic walls, or zero conditions are possible, some of the coefficients a_i in (23) and (24) are altered or vanish.

After determining the coefficients in (23) and (24) for all points P of a waveguide structure and combining the equations, a linear eigenvalue problem of the form

$$\mathbf{A}\cdot\mathbf{H}\equiv\begin{bmatrix}\mathbf{A_{xx}}&\mathbf{A_{xy}}\\\mathbf{A_{yx}}&\mathbf{A_{yy}}\end{bmatrix}\cdot\begin{bmatrix}\mathbf{H_x}\\\mathbf{H_y}\end{bmatrix}=\beta^2\begin{bmatrix}\mathbf{H_x}\\\mathbf{H_y}\end{bmatrix}\equiv\beta^2\mathbf{H}\tag{25}$$

follows [12]. The submatrix $\mathbf{A_{xx}}$ contains the coefficients a_{xxi} and links the neighboring H_x-values, analogously to this the

Authorized licensed use limited to: CAMBRIDGE UNIV. Downloaded on May 25,2020 at 12:09:14 UTC from IEEE Xplore. Restrictions apply.

submatrix $\mathbf{A_{yy}}$ contains the coefficients a_{yyi} of the difference equation (24). H_x and H_y are coupled at plane interfaces by the elements of $\mathbf{A_{xy}}$ and $\mathbf{A_{yx}}$. If $\varepsilon_1 = \varepsilon_2 = \varepsilon_3 = \varepsilon_4$ in Fig. 2, the difference equations for H_x and H_y are not coupled, hence, all the respective elements of $\mathbf{A_{xy}}$ and $\mathbf{A_{yx}}$ are zero.

The eigenvalue problem (25) is solved by an iterative algorithm [13]. The most time consuming part thereby is the matrix-vector product to be formed in each iteration. More precisely it is the multiplication of the submatrice $\mathbf{A_{xx}}$ with $\mathbf{H_x}$ and of $\mathbf{A_{yy}}$ with $\mathbf{H_y}$. Independent of the geometric form of the waveguide considered, all non-zero elements of theses submatrices are aligned in five diagonals due to the used difference star. To achieve high performance for $\mathbf{A_{xx}} \times \mathbf{H_x}$ and $\mathbf{A_{yy}} \times \mathbf{H_y}$ these operations have to be feasible for pipelining, or on vector computers for vectorization. Pipelining and/or vectorization is most efficient, if the elements to be processed are stored in consecutive order. Therefore $\mathbf{A_{xx}}$ and $\mathbf{A_{yy}}$ are stored and processed along diagonals including spreaded elements equal to zero. This technique even saves memory space compared to sparse methods where the indices of the elements have to be stored. The elements in $\mathbf{A_{xy}}$ and $\mathbf{A_{yx}}$ are very few and do only have minor influence on the computing time. They are stored and processed using sparse techniques.

After computing the transverse components H_x and H_y the longitudinal components H_z and E_z can be computed by (8) and (10), respectively. The transverse electric field components E_x and E_y can be determined with curl $\vec{H} = j\omega\varepsilon_0\varepsilon\vec{E}$. Substituting H_z from (8) we obtain, in cartesian coordinates,

$$E_x = \frac{\beta}{\varepsilon k}\sqrt{\frac{\mu_0}{\varepsilon_0}}H_y - \frac{1}{\varepsilon k\beta}\sqrt{\frac{\mu_0}{\varepsilon_0}}\left\{\frac{\partial^2 H_x}{\partial x \partial y} + \frac{\partial^2 H_y}{\partial y^2}\right\} \quad (26)$$

and

$$E_y = -\frac{\beta}{\varepsilon k}\sqrt{\frac{\mu_0}{\varepsilon_0}}H_x + \frac{1}{\varepsilon k\beta}\sqrt{\frac{\mu_0}{\varepsilon_0}}\left\{\frac{\partial^2 H_x}{\partial x^2} + \frac{\partial^2 H_y}{\partial x \partial y}\right\}. \quad (27)$$

In conculsion, we have shown that all six components of the electromagnetic field can be calculated by the finite difference method.

III. Numerical Results

A. Step-Index Fiber

In every finite-difference approach, three approximations are made [6]. First, the differential equations (2) and (3) are replaced by the difference equations (19) and (21). Secondly, contours not parallel to lines of the grid, have to be approximated by stair cases in order to be able to treat the problem with a rectangular mesh, as sketched in Fig. 2. Finally, even the iterative equation solver causes an additional error.

To illustrate the accuracy of our numerical solutions, let us now compare them with the well known analytical solution of a step-index fiber. We selected a fiber with core diameter 9-μm, core refractive index $n_1 = 3.4147700$ (InGaAsP, $\lambda_g = 1.3$ μm [14]) and cladding index $n_2 = 3.1658900$ (InP [14]), which simulates the refractive index properties of integrated optics devices. The more critical case of a large refractive index step typical for integrated optics was selected because we wanted to show that the error made by the step-like approximation of the round contour is here negligible even for a moderate number of mesh points. For $\lambda = 1.3$ μm the analytical solution for the fundamental mode is $\beta_0/k = n_{\text{eff,ana}} = 3.4130933...$, which can be obtained by solving the characteristic equation containing Bessel functions J and K [15].

TABLE I
Effective Index β/k of the Fundamental Mode of a Step-Index Fiber for Different Mesh Intervals dx and Sizes W of the Computation Window. $N_{x,y}$ is the Number of Discretization Points in x- and y-Direction. The Last Column Contains the Relative Error, Where β_0 is the Analytical Solution for the Step-Index Fiber.

	W/μm	$N_{x,y}$	$dx, dy/\mu$m	β/k	$(\beta - \beta_0)/\beta_0$
1	40	109	0.25 ... 0.78	3.4130576	$-1.0\cdot10^{-5}$
2	40	161	0.17 ... 0.54	3.4130741	$-5.6\cdot10^{-6}$
3	40	217	0.13 ... 0.39	3.4130765	$-4.9\cdot10^{-6}$
4	40	261	0.10 ... 0.35	3.4130888	$-1.3\cdot10^{-6}$
5	35	245	0.10 ... 0.31	3.4130888	$-1.3\cdot10^{-6}$
6	30	227	0.10 ... 0.27	3.4130888	$-1.3\cdot10^{-6}$
7	25	207	0.10 ... 0.22	3.4130888	$-1.3\cdot10^{-6}$
8	20	199	0.10 ... 0.11	3.4130888	$-1.3\cdot10^{-6}$
9	20	223	0.09 ... 0.10	3.4130892	$-1.2\cdot10^{-6}$
10	20	247	0.08 ... 0.09	3.4130895	$-1.1\cdot10^{-6}$
11	20	263	0.07 ... 0.10	3.4130918	$-4.3\cdot10^{-7}$

Table I lists several numerical results for the step-index fiber obtained for different mesh intervals and sizes of the computational window. These results are compared with the analytical solution by the relative error, which is given in the last column of Table I. In all computations the central part of the waveguide was scanned with a uniform mesh with constant $dx = dy$, given as the smaller value in the respective column of Table I. Towards the boundary, the mesh size was increased up to the larger limit in Table I. As the number of discretization points $N_{x,y}$ increases form 109 in row 1 to 261 in row 4, the relative error decreases by a factor of 10. The results in the next four rows show that the value of the effective index β/k is not affected, if the computational window is reduced from 40 μm $\times$ 40 μm to 20 μm $\times$ 20 μm. A further reduction of the relative error by a factor of three is achieved by decreasing the mesh interval in the center region of the $(20\ \mu\text{m})^2$ computational window from 0.1 μm to 0.07 μm, which is shown in the last four rows of Table I. The numerical solution with a 0.071-μm spacing of the mesh points gives $n_{\text{eff,num}} = 3.4130918$. This corresponds to the very small relative error of $(n_{\text{eff,num}} - n_{\text{eff,ana}})/n_{\text{eff,ana}} \simeq -4.4 \times 10^{-7}$ for the high index difference of 7.3%. Fig. 4 shows the analytical and numerically calculated components H_x and H_y, it demonstrates the great dynamic range of our method.

B. Rib Waveguide with Large Refractive Index Steps

The rib waveguide sketched in Fig. 5 has been analyzed by several authors [16]–[20] with different methods. Table

Authorized licensed use limited to: CAMBRIDGE UNIV. Downloaded on May 25,2020 at 12:09:14 UTC from IEEE Xplore. Restrictions apply.

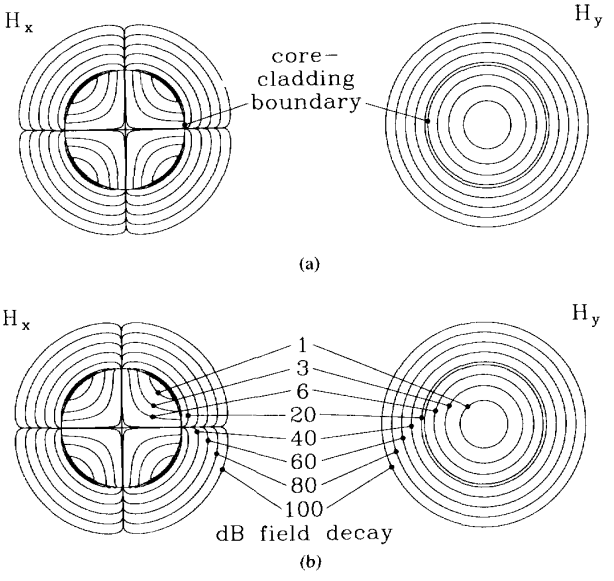

Fig. 4. Transverse magnetic field of the x-polarized fundamental mode of a step-index fiber. (a) Computed with an analytical formulation in terms of Bessel functions J and K [15]. (b) Results obtained with the new finite difference method (see row 11 of Table I).

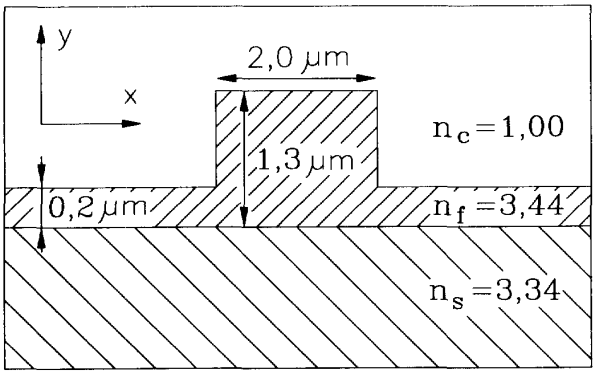

Fig. 5. Rib waveguide with large refractive index steps.

II summarizes the results for the effective index β/k of the fundamental mode, which corresponds to the HE-polarization of the hybrid field or the TE-modes in the case of scalar or semivectorial methods. To compare the results, Table II lists the difference of the effective indices $(\beta_i - \beta_{16})/k$, where β_{16}/k is the effective index obtained by our finite difference method with a dense mesh of 508×394 mesh points. The transverse magnetic field components calculated for this example are shown in Fig. 6.

First of all, we will discuss the results obtained for different effective index methods (EIM) that are listed in the first three rows of Table II. A difficulty for the EIM is caused the fact that for $\lambda = 1.55$ μm the 0.2 μm dielectric slab does not guide any mode and hence no effective index can be calculated for it. If we nevertheless want to apply the EIM, we must

TABLE II
EFFECTIVE INDEX β/k OF THE FUNDAMENTAL MODE OF THE RIB WAVEGUIDE SKETCHED IN FIG. 5 COMPUTED BY DIFFERENT METHODS FOR λ = 1.55 μm. dx DENOTES THE SPACING OF THE MESH POINTS. THE LAST COLUMN LISTS THE DEVIATIONS FROM OUR CALCULATION NO. 16.

i	Method	dx/μm	β_i/k	$(\beta_i - \beta_{16})/k$
1	EIM TE-TM N_S = 1.0 this work	—	3.387597	$-1.1\cdot10^{-3}$
2	EIM TE-TM $\overline{N_S}$ this work	—	3.388915	$2.3\cdot10^{-4}$
3	EIM TE-TE N_S = 1.0 Robertson [16]	—	3.390322	$1.6\cdot10^{-3}$
4	scalar FDM1 Robertson [16]	0.033	3.390618	$1.9\cdot10^{-3}$
5	scalar FDM2 Robertson [16]	0.033	3.391292	$2.6\cdot10^{-3}$
6	scalar FDM Delâge [17]	0.025	3.391320	$2.6\cdot10^{-3}$
7	semivectorial FDM Stern [18]	0.095	3.386926	$-1.8\cdot10^{-3}$
8	semivectorial FDM Vasallo [19]	0.010	3.388669	$-1.8\cdot10^{-5}$
9	mode matching technique Rozzi [20]	—	3.388690	$3.0\cdot10^{-6}$
10	vectorial FDM this work	0.100	3.388120	$-5.7\cdot10^{-4}$
11	"	0.063	3.388420	$-2.7\cdot10^{-4}$
12	"	0.042	3.388584	$-1.0\cdot10^{-4}$
13	"	0.025	3.388655	$-3.2\cdot10^{-5}$
14	"	0.020	3.388671	$-1.6\cdot10^{-5}$
15	"	0.016	3.388680	$-7.0\cdot10^{-6}$
16	"	0.013	3.388687	0

select a suitable value for this effective index N_S, but the choice will remain somehow arbitrary. Setting the effective index $N_s = 1.0$ in the regions neighboring the ridge, gives the results shown in the first row of Table II. The effective index β_1/k is much lower than the value from calculation 16. Using an average effective index $\overline{N_S} = 0.5(n_s + n_c)$ in these regions instead, reduces the absolute value of the deviation by a factor of ≈ 5. To obtain these results, we have first solved the characteristic equation in the vertical direction for the TE-polarization. In a second step, the three effective indices of the structure form an eigenvalue problem for the equivalent slab structure in horizontal direction. Here, a characteristic equation for the TM-polarization has to be solved. Contrary to that Robertson [16] used two times the characteristic equation for the TE-polarization, which we found out by reproducing the value β_3/k given in [16]. Using two times the TE-equation is a false approach and results, compared to our EIM's, in a larger deviation from the more accurate effective index of our finite difference method.

Scalar finite difference methods calculate only the dominant field component using one scalar Helmholtz equation; they ignore the refractive index steps and the hybrid nature of

Authorized licensed use limited to: CAMBRIDGE UNIV. Downloaded on May 25,2020 at 12:09:14 UTC from IEEE Xplore. Restrictions apply.

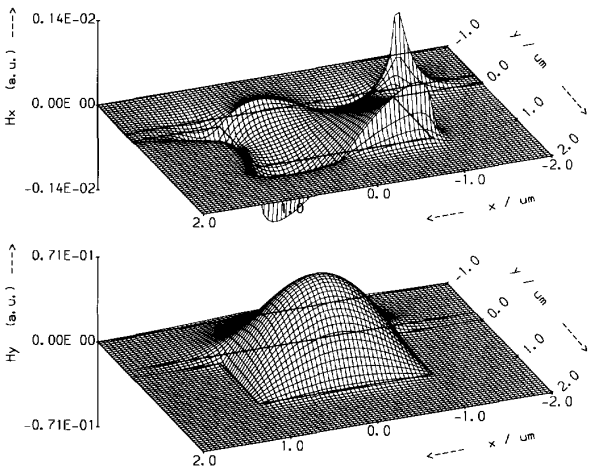

Fig. 6. Tranverse magnetic field of the fundamental mode of the rib waveguide of Fig. 5. Only a part of the 8-μm $\times$ 6-μm-large computational window is shown.

the field. In Table II, rows 4–6, different scalar finite differnces methods are compared with our vectorial method. The methods differ in how they treat the refractive index steps. In Robertson's FDM1 [16] and Delâge's FDM [17] the grid points are lying on the boundaries, whereas in the second FDM of Robertson the index steps always lies between two grid points. This does not improve the accuracy of the solution and the deviations in the last column are the largest of the entire table. Therefore, scalar finite difference methods are no better than effective index methods for the rib waveguide with large refractive index steps.

The semivectorial FDM's of Stern [18] and Vasallo [19] and the 'mode matching technique' of Rozzi [20] consider the boundary conditions for dielectric index steps. The result of Stern, calculated on a coarse mesh, still deviates much from ours. The value given by Vasallo and also the result of the analytical mode matching technique of Rozzi agree well with our result. However, in the current implementation, these methods neglect the small hybrid components of the fields. In consequence, polarization converting devices and other waveguide components with highly hybrid fields cannot be analyzed by these methods.

Columns 10–16 of Table II show how our results change with decreasing mesh size. The uniform mesh size $dx = dy$ for the central part of the rib is given in the table. Outside the central region we used a mesh with increasing size, where the largest mesh size, occuring at the boundary of the computational window, is approximately twice the value appearing in the table. Even with the coarse mesh ($dx = 0.1$ μm) the deviation of $-5.7 \cdot 10^{-4}$ is approximately one order of magnitude smaller than the deviations calculated for the scalar schemes of Robertson and Delâge. The semivectorial method of Stern (number 7) is more accurate. With approximately equal meshes, the deviation of Stern's method is approximately three times larger than of our vectorial method (calculation 10).

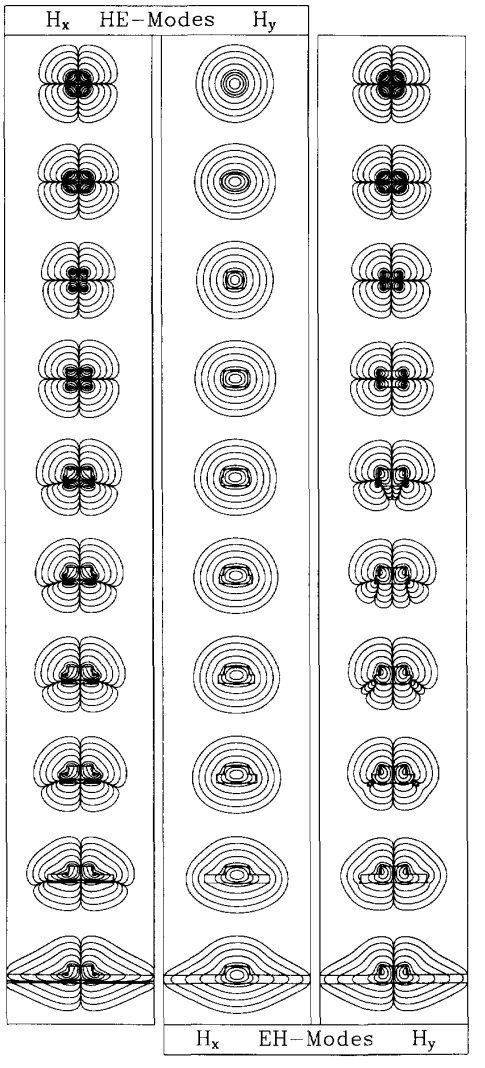

Fig. 7. Evolution ofthe transverse magnetic field of the HE- and EH-mode from a step index fiber to a buried rib waveguide. Contour lines of the transverse magnetic field components are shown at 1- , 3- , 6- , 10- , 20- , 30- , 40- , and 50-dB field decay.The left column shows the weak component $H_x$of the HE-mode, the right column H_y of the EH-mode. Because within the solution of the plots the dominant components of the two polarizations cannot be distinguished, only one plot needs to be given (center column). The dominant field components are appoximately 200 times larger than the weak components.

C. Vectorial Mode-Fields of Ridge-Waveguides

To demonstrate how the field distributions change when a buried square channel waveguide evolves into a buried rib waveguide, we have selected typical refractive indices as they occur in opto-electronics, namely InGaAsP ($n_1 = 3.2615$ at $\lambda_g = 1.05$ μm [14]) for the guiding section and InP ($n_2 = 3.1659$) for substrate and cladding at a wavelength of $\lambda = 1.55$ μm. The first row of Fig. 7 shows a buried channel guide, for which the complete transverse magnetic field has already been published [21]. As the buried waveguide evolves into

Authorized licensed use limited to: CAMBRIDGE UNIV. Downloaded on May 25,2020 at 12:09:14 UTC from IEEE Xplore. Restrictions apply.

the rib waveguide, the weak transverse components (H_x for the HE-polarization and H_y for the EH-polarization) behave differently for the two polarizations. The weak component H_x of the HE-polarization retains its two zero crossings, whereas the weak component H_y of the EH-polarization loses it's zero crossing in the y-direction. A part of Fig. 7 was recently presented as a preliminary result [8].

IV. Conclusion

In conclusion, a new *unique* set of difference equations is derived. This is achieved by an accurate formulation of the boundary conditions. The new finite difference scheme differs from other methods in the dynamic range. The very high dynamic range of our method allows the weak transverse field components to be calculated. Due to the great dynamic range, it was possible to calculate the weak components of the hybrid field of dielectric rib waveguides. Also, the accuracy of our method is high. This has been shown by a comparison of the numerical results with the analytical solution for a step-index fiber. In this example, the relative error in the propagation constant is as low as 4.4×10^{-7} for an index difference of 7.3%. For a rib waveguide we have compared our results with previously published data based on other methods. We have found that two semivectorial methods agree well with our results, while for scalar schemes and EIMs considerable deviations occur.

Acknowledgment

The authors would like to acknowledge suggestions and help given by W. Höfle regarding the presentation of the material and the preparation of the final manuscript.

References

[1] T. L. Koch and U. Koren, "Semiconductor Photonic Integrated Circuits," *IEEE J. Quantum Electron.*, vol. 27, pp. 641–653, 1991.
[2] H. Takeuchi, K. Kasaya, Y. Kondo, H. Yasaka, K. Oe, and Y. Imamura, "Monolithic Integrated Coherent Receiver on InP Substrate," *IEEE Photon. Technol. Lett.*, vol. 26, pp. 142–143, 1990.
[3] W. Schlosser, "Der rechteckige dielektrische Draht," *Arch. Elek. Übertragung*, vol. 18, pp. 403–410, 1964.
[4] J. E. Goell, "A circular-harmonic computer analysis of rectangular dielectric waveguides," *Bell Syst. Tech. J.*, vol. 48, pp. 2133–2160, 1969.
[5] J. B. Davies and C. A. Muilwyk, "Numerical Solution of uniform hollow waveguides of arbitrary shape," in *Proc. Inst. Elec. Eng.*, 1966, vol. 113, pp. 277–284.
[6] A. Wexler, "Computation of Electromagnetic Fields," *IEEE Trans. Microwave Theory Tech.*, vol. 17, pp. 416–439, 1969.
[7] K. Bierwirth, N. Schulz, and F. Arndt, "Finite-Difference Analysis of Rectangular Dielectric Waveguide Structures," *IEEE Trans. Microwave Theory Tech.*, vol. 34, pp. 1104–1113, 1986.
[8] P. Lüsse, P. Stuwe, J. Schüle, and H.-G. Unger, "Vectorial Finite-Difference Approach for Optical Waveguides," in *Proc. ECIO'93*, 1993, Neuchatel.
[9] C.-C. Su, "Origin of Spurious Modes in the Analysis of Optical Fibre Using the Finite-Element of Finite-Difference Technique," *Electron. Lett.*, vol. 21, pp. 858–860, 1985.
[10] N. Schulz, K. Bierwirth, and F. Arndt, "Finite Difference Analysis of Integrated Optical Waveguides without Spurious Mode Solution," *Electron. Lett.*, vol. 22, pp. 963–965, 1986.
[11] H. R. Schwarz, *Numerische Mathematik*. Stuttgart: *Teubner Verlag*,1988.
[12] P. Stuwe, "Passive Wellenleiterbauelemente für den optoelektronisch integrierten Teilnehmeranschluß," *Fortschritt-Berichte* VDI, series 10, no. 252, Düsseldorf, 1993.
[13] W. J. Stewart and A. Jennings, "A Simultaneous Iteration Algorithm for Real Matrices," *ACM Trans. Math. Softw.*, vol. 7, pp. 184–198, 1981.
[14] F. Fiedler and A. Schlachetzki, "Optical parameters of InP-based waveguides," *Solid State Commun.*, vol. 30, pp. 73–83, 1987.
[15] b
[16] H.-G. Unger, *Planar Optical Waveguides*. Oxford: Clarendon Press, 1977.
[17] M. J. Robertson, S. Ritchie, and P. Dayan, "Semiconductor waveguides: analysis of optical propagation in single rib structures and directional couplers," in *Proc. Inst. Elec. Eng.*, 1985, vol. 132, pt. J, pp. 336–342.
[18] A. Delâge, "Modelling of semiconductor rib wave guides by a finite difference method," *Can. J. Phys.*, vol. 69, pp. 512–519, 1991.
[19] M. S. Stern, "Semivectorial polarised finite difference method for optical waveguides with arbitrary index profiles," in *Proc. Inst. Elec. Eng.*, 1988, pt. J, vol. 135, pp. 56–63.
[20] A. Vasallo, "Improved Finite Difference Derivation of Semi-Vectorial Modes in 3D Step-Index Waveguides," in *Proc. vol. I, 18th European Conf. on Optical Commun.*,, 1992, Berlin, paper We P2.25, pp. 565–568
[21] T. Rozzi, G. Cerri, M. N. Husain, and L. Zappelli, "Variational analysis of the dielectric rib waveguide using the concept of "Transition Function" and including edge singularities," *IEEE Trans. Microwave Theory Tech.*, vol. 39, pp. 247–256, 1991.
[22] W. P. Huang, C. L. Xu, and S. K. Chaudhuri, "A vector beam propagation method based on H fields," *IEEE Photon. Technol. Lett.*, vol. 3, pp. 1117–1120, 1991.

Paul Lüsse (S'93) was born in Emstek, Germany in August 1965. He received the diploma degree in electrical engineering from the Technical University of Braunschweig in 1992. Since then, he is a research assistant at the institute of RF engineering (Institut für Hochfrequenztechnik). His research interests are single mode fibers, integrated optics, numerical methods for optical waveguides and MQW-structures.

Peter Stuwe (M'93) was born in Detmold, Germany, in June 1961. He received the diploma degree in electrical engineering from the Technical University of Braunschweig in 1988. Subsequently he was a research assistant at the institute of RF engineering (Institut für Hochfrequenztechnik) where he worked on the analysis of various semiconductor devices for the optoelectronic integrated subscriber terminal. A main part of his research work concerned the improvement of numerical methods for the calculation of electromagnetic mode fields. He obtained his doctoral degree in electrical engineering from the Technical University of Braunschweig in 1993. Since March 1993 he works in the field of RF electronics at the radio communication division of Robert Bosch GmbH, Bosch Telecom.

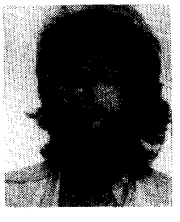

Josef Schüle was born in Stühlingen, Germany, in August 1960. He received his doctorate in chemistry from the university of Münster in 1986. Between 1986 and 1989, he held postdoctoral positions in theoretical physics and physical chemistry at the universities of Stockholm and Berlin (FU). He assumed his current research position as staff member of the Computing Center of the Technical University of Braunschweig in 1989. His current interests include the vectorization and parallelization of eigenvalue problems.

Authorized licensed use limited to: CAMBRIDGE UNIV. Downloaded on May 25,2020 at 12:09:14 UTC from IEEE Xplore. Restrictions apply.

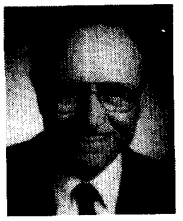

Hans-Georg Unger (M'56-SM'59-F'74-LF'92) received a diploma degree and a Dr.-Ing. degree in electrical engineering from the Technical University of Braunschweig in 1951 and 1954, respectively. From 1951 to 1955 he was research engineer and head of microwave research at Siemens in Munich, Germany. From 1956 to 1960 he was a member of the technical staff and head of a research department at the AT&T Bell Laboratories in Holmdel and Murray Hill, NJ (USA). Since 1960 he is professor of electrical engineering at the Technical University of Braunschweig and head of the department of RF engineering (Institut für Hochfrequenztechnik). He received honorary doctor degrees (Dr.-Ing. E. h.) from the Technical University of Munich (1985), the University of Ulm (1992) and (Dr. rer. nat. h. c.) from the Technical University of Hamburg–Harburg (1993). In 1988 he was awarded the IEEE Heinrich Hertz Medal. Since 1990 he is a Foreign Member of the Polish Academy of Sciences. His current research interest are integrated photonics and microwave antennas.

Authorized licensed use limited to: CAMBRIDGE UNIV. Downloaded on May 25,2020 at 12:09:14 UTC from IEEE Xplore. Restrictions apply.